First measurement of the charged current $\bar{\nu}_\mu$ double differential cross section on a water target without pions in the final state

K. Abe,[1] R. Akutsu,[2] A. Ali,[3] C. Alt,[4] C. Andreopoulos,[5,6] L. Anthony,[6] M. Antonova,[7] S. Aoki,[8] A. Ariga,[9] Y. Ashida,[3] E. T. Atkin,[10] Y. Awataguchi,[11] S. Ban,[3] M. Barbi,[12] G. J. Barker,[13] G. Barr,[14] C. Barry,[6] M. Batkiewicz-Kwasniak,[15] A. Beloshapkin,[16] F. Bench,[6] V. Berardi,[17] S. Berkman,[18,19] L. Berns,[20] S. Bhadra,[21] S. Bienstock,[22] A. Blondel,[23,‖] S. Bolognesi,[24] B. Bourguille,[25] S. B. Boyd,[13] D. Brailsford,[26] A. Bravar,[23] C. Bronner,[1] M. Buizza Avanzini,[27] J. Calcutt,[28] T. Campbell,[29] S. Cao,[30] S. L. Cartwright,[31] M. G. Catanesi,[17] A. Cervera,[7] A. Chappell,[13] C. Checchia,[32] D. Cherdack,[33] N. Chikuma,[34] G. Christodoulou,[35] J. Coleman,[6] G. Collazuol,[32] L. Cook,[14,36] D. Coplowe,[14] A. Cudd,[28] A. Dabrowska,[15] G. De Rosa,[37] T. Dealtry,[26] P. F. Denner,[13] S. R. Dennis,[6] C. Densham,[5] F. Di Lodovico,[38] N. Dokania,[39] S. Dolan,[35] O. Drapier,[27] J. Dumarchez,[22] P. Dunne,[10] L. Eklund,[40] S. Emery-Schrenk,[24] A. Ereditato,[9] P. Fernandez,[7] T. Feusels,[18,19] A. J. Finch,[26] G. A. Fiorentini,[21] G. Fiorillo,[37] C. Francois,[9] M. Friend,[30,¶] Y. Fujii,[30,¶] R. Fujita,[34] D. Fukuda,[41] R. Fukuda,[42] Y. Fukuda,[43] K. Gameil,[18,19] C. Giganti,[22] T. Golan,[44] M. Gonin,[27] A. Gorin,[16] M. Guigue,[22] D. R. Hadley,[13] J. T. Haigh,[13] P. Hamacher-Baumann,[45] M. Hartz,[19,36] T. Hasegawa,[30,¶] N. C. Hastings,[30] T. Hayashino,[3] Y. Hayato,[1,36] A. Hiramoto,[3] M. Hogan,[46] J. Holeczek,[47] N. T. Hong Van,[48,49] F. Iacob,[32] A. K. Ichikawa,[3] M. Ikeda,[1] T. Ishida,[30,¶] T. Ishii,[30,¶] M. Ishitsuka,[42] K. Iwamoto,[34] A. Izmaylov,[7,16] B. Jamieson,[50] S. J. Jenkins,[31] C. Jesús-Valls,[25] M. Jiang,[3] S. Johnson,[29] P. Jonsson,[10] C. K. Jung,[39,†] M. Kabirnezhad,[14] A. C. Kaboth,[51,5] T. Kajita,[2,†] H. Kakuno,[11] J. Kameda,[1] D. Karlen,[52,19] Y. Kataoka,[1] T. Katori,[38] Y. Kato,[1] E. Kearns,[53,36,†] M. Khabibullin,[16] A. Khotjantsev,[16] H. Kim,[54] J. Kim,[18,19] S. King,[55] J. Kisiel,[47] A. Knight,[13] A. Knox,[26] T. Kobayashi,[30,¶] L. Koch,[5] T. Koga,[34] A. Konaka,[19] L. L. Kormos,[26] Y. Koshio,[41,†] K. Kowalik,[56] H. Kubo,[3] Y. Kudenko,[16,‡] N. Kukita,[54] R. Kurjata,[57] T. Kutter,[58] M. Kuze,[20] L. Labarga,[59] J. Lagoda,[56] M. Lamoureux,[32] M. Laveder,[32] M. Lawe,[26] M. Licciardi,[27] T. Lindner,[19] R. P. Litchfield,[40] S. L. Liu,[39] X. Li,[39] A. Longhin,[32] L. Ludovici,[60] X. Lu,[14] T. Lux,[25] L. Magaletti,[17] K. Mahn,[28] M. Malek,[31] S. Manly,[61] L. Maret,[23] A. D. Marino,[29] J. F. Martin,[62] T. Maruyama,[30,¶] T. Matsubara,[30] K. Matsushita,[34] V. Matveev,[16] K. Mavrokoridis,[6] E. Mazzucato,[24] M. McCarthy,[21] N. McCauley,[6] K. S. McFarland,[61] C. McGrew,[39] A. Mefodiev,[16] C. Metelko,[6] M. Mezzetto,[32] A. Minamino,[63] O. Mineev,[16] S. Mine,[64] M. Miura,[1,†] L. Molina Bueno,[4] S. Moriyama,[1,†] J. Morrison,[28] Th. A. Mueller,[27] L. Munteanu,[24] S. Murphy,[4] Y. Nagai,[29] T. Nakadaira,[30,¶] M. Nakahata,[1,36] Y. Nakajima,[1] A. Nakamura,[41] K. G. Nakamura,[3] K. Nakamura,[36,30,¶] S. Nakayama,[1,36] T. Nakaya,[3,36] K. Nakayoshi,[30,¶] C. Nantais,[62] T. V. Ngoc,[48] K. Niewczas,[44] K. Nishikawa,[30,*] Y. Nishimura,[65] T. S. Nonnenmacher,[10] F. Nova,[5] P. Novella,[7] J. Nowak,[26] J. C. Nugent,[40] H. M. O'Keeffe,[26] L. O'Sullivan,[31] K. Okumura,[2,36] T. Okusawa,[54] S. M. Oser,[18,19] R. A. Owen,[55] Y. Oyama,[30,¶] V. Palladino,[37] J. L. Palomino,[39] V. Paolone,[66] W. C. Parker,[51] P. Paudyal,[6] M. Pavin,[19] D. Payne,[6] G. C. Penn,[6] L. Pickering,[28] C. Pidcott,[31] E. S. Pinzon Guerra,[21] C. Pistillo,[9] B. Popov,[22,§] K. Porwit,[47] M. Posiadala-Zezula,[67] A. Pritchard,[6] B. Quilain,[36] T. Radermacher,[45] E. Radicioni,[17] B. Radics,[4] P. N. Ratoff,[26] E. Reinherz-Aronis,[46] C. Riccio,[37] E. Rondio,[56] S. Roth,[45] A. Rubbia,[4] A. C. Ruggeri,[37] A. Rychter,[57] K. Sakashita,[30,¶] F. Sánchez,[23] C. M. Schloesser,[4] K. Scholberg,[68,†] J. Schwehr,[46] M. Scott,[10] Y. Seiya,[54,††] T. Sekiguchi,[30,¶] H. Sekiya,[1,36,†] D. Sgalaberna,[35] R. Shah,[5,14] A. Shaikhiev,[16] F. Shaker,[50] A. Shaykina,[16] M. Shiozawa,[1,36] W. Shorrock,[10] A. Shvartsman,[16] A. Smirnov,[16] M. Smy,[64] J. T. Sobczyk,[44] H. Sobel,[64,36] F. J. P. Soler,[40] Y. Sonoda,[1] J. Steinmann,[45] S. Suvorov,[16,24] A. Suzuki,[8] S. Y. Suzuki,[30,¶] Y. Suzuki,[36] A. A. Sztuc,[10] M. Tada,[30,¶] A. Takeda,[1] Y. Takeuchi,[8,36] H. K. Tanaka,[1,†] H. A. Tanaka,[69,62] S. Tanaka,[54] L. F. Thompson,[31] W. Toki,[46] C. Touramanis,[6] K. M. Tsui,[6] T. Tsukamoto,[30,¶] M. Tzanov,[58] Y. Uchida,[10] W. Uno,[3] M. Vagins,[36,64] S. Valder,[13] Z. Vallari,[39] D. Vargas,[25] G. Vasseur,[24] C. Vilela,[39] W. G. S. Vinning,[13] T. Vladisavljevic,[14,36] V. V. Volkov,[16] T. Wachala,[15] J. Walker,[50] J. G. Walsh,[26] Y. Wang,[39] D. Wark,[5,14] M. O. Wascko,[10] A. Weber,[5,14] R. Wendell,[3,†] M. J. Wilking,[39] C. Wilkinson,[9] J. R. Wilson,[38] R. J. Wilson,[46] K. Wood,[39] C. Wret,[61] Y. Yamada,[30,*] K. Yamamoto,[54,††] C. Yanagisawa,[39,**] G. Yang,[39] T. Yano,[1] K. Yasutome,[3] S. Yen,[19] N. Yershov,[16] M. Yokoyama,[34,†] T. Yoshida,[20] M. Yu,[21] A. Zalewska,[15] J. Zalipska,[56] K. Zaremba,[57] G. Zarnecki,[56] M. Ziembicki,[57] E. D. Zimmerman,[29] M. Zito,[24] S. Zsoldos,[55] and A. Zykova[16]

(The T2K Collaboration)

[1]*University of Tokyo, Institute for Cosmic Ray Research, Kamioka Observatory, Kamioka, Japan*
[2]*University of Tokyo, Institute for Cosmic Ray Research, Research Center for Cosmic Neutrinos, Kashiwa, Tokyo, Japan*
[3]*Kyoto University, Department of Physics, Kyoto, Japan*
[4]*ETH Zurich, Institute for Particle Physics, Zurich, Switzerland*

[5]*STFC, Rutherford Appleton Laboratory, Harwell Oxford, and Daresbury Laboratory, Warrington, United Kingdom*
[6]*University of Liverpool, Department of Physics, Liverpool, United Kingdom*
[7]*IFIC (CSIC & University of Valencia), Valencia, Spain*
[8]*Kobe University, Kobe, Japan*
[9]*University of Bern, Albert Einstein Center for Fundamental Physics, Laboratory for High Energy Physics (LHEP), Bern, Switzerland*
[10]*Imperial College London, Department of Physics, London, United Kingdom*
[11]*Tokyo Metropolitan University, Department of Physics, Tokyo, Japan*
[12]*University of Regina, Department of Physics, Regina, Saskatchewan, Canada*
[13]*University of Warwick, Department of Physics, Coventry, United Kingdom*
[14]*Oxford University, Department of Physics, Oxford, United Kingdom*
[15]*H. Niewodniczanski Institute of Nuclear Physics PAN, Cracow, Poland*
[16]*Institute for Nuclear Research of the Russian Academy of Sciences, Moscow, Russia*
[17]*INFN Sezione di Bari and Università e Politecnico di Bari, Dipartimento Interuniversitario di Fisica, Bari, Italy*
[18]*University of British Columbia, Department of Physics and Astronomy, Vancouver, British Columbia, Canada*
[19]*TRIUMF, Vancouver, British Columbia, Canada*
[20]*Tokyo Institute of Technology, Department of Physics, Tokyo, Japan*
[21]*York University, Department of Physics and Astronomy, Toronto, Ontario, Canada*
[22]*Sorbonne Université, Université Paris Diderot, CNRS/IN2P3, Laboratoire de Physique Nucléaire et de Hautes Energies (LPNHE), Paris, France*
[23]*University of Geneva, Section de Physique, DPNC, Geneva, Switzerland*
[24]*IRFU, CEA Saclay, Gif-sur-Yvette, France*
[25]*Institut de Fisica d'Altes Energies (IFAE), The Barcelona Institute of Science and Technology, Campus UAB, Bellaterra (Barcelona), Spain*
[26]*Lancaster University, Physics Department, Lancaster, United Kingdom*
[27]*Ecole Polytechnique, IN2P3-CNRS, Laboratoire Leprince-Ringuet, Palaiseau, France*
[28]*Michigan State University, Department of Physics and Astronomy, East Lansing, Michigan, USA*
[29]*University of Colorado at Boulder, Department of Physics, Boulder, Colorado, USA*
[30]*High Energy Accelerator Research Organization (KEK), Tsukuba, Ibaraki, Japan*
[31]*University of Sheffield, Department of Physics and Astronomy, Sheffield, United Kingdom*
[32]*INFN Sezione di Padova and Università di Padova, Dipartimento di Fisica, Padova, Italy*
[33]*University of Houston, Department of Physics, Houston, Texas, USA*
[34]*University of Tokyo, Department of Physics, Tokyo, Japan*
[35]*CERN European Organization for Nuclear Research, CH-1211 Genve 23, Switzerland*
[36]*Kavli Institute for the Physics and Mathematics of the Universe (WPI), The University of Tokyo Institutes for Advanced Study, University of Tokyo, Kashiwa, Chiba, Japan*
[37]*INFN Sezione di Napoli and Università di Napoli, Dipartimento di Fisica, Napoli, Italy*
[38]*King's College London, Department of Physics, Strand, London WC2R 2LS, United Kingdom*
[39]*State University of New York at Stony Brook, Department of Physics and Astronomy, Stony Brook, New York, USA*
[40]*University of Glasgow, School of Physics and Astronomy, Glasgow, United Kingdom*
[41]*Okayama University, Department of Physics, Okayama, Japan*
[42]*Tokyo University of Science, Faculty of Science and Technology, Department of Physics, Noda, Chiba, Japan*
[43]*Miyagi University of Education, Department of Physics, Sendai, Japan*
[44]*Wroclaw University, Faculty of Physics and Astronomy, Wroclaw, Poland*
[45]*RWTH Aachen University, III. Physikalisches Institut, Aachen, Germany*
[46]*Colorado State University, Department of Physics, Fort Collins, Colorado, USA*
[47]*University of Silesia, Institute of Physics, Katowice, Poland*
[48]*Institute For Interdisciplinary Research in Science and Education (IFIRSE), ICISE, Quy Nhon, Vietnam*
[49]*International Centre of Physics, Institute of Physics (IOP), Vietnam Academy of Science and Technology (VAST), 10 Dao Tan, Ba Dinh, Hanoi, Vietnam*
[50]*University of Winnipeg, Department of Physics, Winnipeg, Manitoba, Canada*
[51]*Royal Holloway University of London, Department of Physics, Egham, Surrey, United Kingdom*
[52]*University of Victoria, Department of Physics and Astronomy, Victoria, British Columbia, Canada*
[53]*Boston University, Department of Physics, Boston, Massachusetts, USA*
[54]*Osaka City University, Department of Physics, Osaka, Japan*

[55]Queen Mary University of London, School of Physics and Astronomy, London, United Kingdom
[56]National Centre for Nuclear Research, Warsaw, Poland
[57]Warsaw University of Technology, Institute of Radioelectronics and Multimedia Technology, Warsaw, Poland
[58]Louisiana State University, Department of Physics and Astronomy, Baton Rouge, Louisiana, USA
[59]University Autonoma Madrid, Department of Theoretical Physics, 28049 Madrid, Spain
[60]INFN Sezione di Roma and Università di Roma "La Sapienza," Roma, Italy
[61]University of Rochester, Department of Physics and Astronomy, Rochester, New York, USA
[62]University of Toronto, Department of Physics, Toronto, Ontario, Canada
[63]Yokohama National University, Faculty of Engineering, Yokohama, Japan
[64]University of California, Irvine, Department of Physics and Astronomy, Irvine, California, USA
[65]Keio University, Department of Physics, Kanagawa, Japan
[66]University of Pittsburgh, Department of Physics and Astronomy, Pittsburgh, Pennsylvania, USA
[67]University of Warsaw, Faculty of Physics, Warsaw, Poland
[68]Duke University, Department of Physics, Durham, North Carolina, USA
[69]SLAC National Accelerator Laboratory, Stanford University, Menlo Park, California, USA

(Received 28 August 2019; accepted 24 June 2020; published 21 July 2020)

This paper reports the first differential measurement of the charged-current $\bar{\nu}_\mu$ interaction cross section on water with no pions in the final state. The unfolded flux-averaged measurement using the T2K off-axis near detector is given in double-differential bins of μ^+ momentum and angle. The integrated cross section in a restricted phase space is $\sigma = (1.11 \pm 0.18) \times 10^{-38}$ cm^2 per water molecule. Comparisons with several nuclear models are also presented.

DOI: 10.1103/PhysRevD.102.012007

I. INTRODUCTION

Long-baseline neutrino experiments [1,2] are now measuring both neutrino ($\nu_\mu \to \nu_e$) and antineutrino ($\bar{\nu}_\mu \to \bar{\nu}_e$) appearance oscillations to determine fundamental neutrino mixing parameters and to search for charge-parity (CP) violation in the lepton sector. Testing this symmetry may answer one of the most fundamental physics questions: the mystery of the matter-antimatter imbalance in our Universe.

Neutrino oscillation measurements are performed by measuring neutrino interactions on nuclei. The present uncertainties on models describing the (anti)neutrino-nucleus scattering are the main source of systematic error in currently operating experiments [such as Tokai to Kamioka (T2K) [3] and NOvA [4]] and will affect future projects (such as DUNE [5] and HyperKamiokande [6]). The main difficulty in the description of (anti)neutrino-nucleus interactions derives from the intrinsic nature of the nucleus, where nucleons are bound together and nuclear effects must be taken into account. Many models are currently available that describe different pieces of this complex scenario, such as the relativistic Fermi gas [7], spectral function [8,9], random phase approximation [10–13], and multinucleon models [14–24]. Thus, a key component required by present and future [5,25] experiments are the precise measurements and tests of theoretical models of both neutrino and antineutrino cross sections on detector target materials, such as scintillator, water, and liquid argon. In charged-current (CC) interactions without pions in the final state, detailed measurements of the outgoing muon will help to test different theoretical models. In this paper, using the off-axis near detector of the T2K experiment, we present the first double-differential antineutrino cross section measurement on water and compare it to various model predictions.

Measurements by T2K probe the completeness of the interaction model by comparing neutrinos and antineutrinos [26], by using different target materials [27,28] and different energy spectra [29–31], and through leptonic-hadronic state correlations [32]. The published T2K measurements used unfolding techniques, such as D'Agostini's iterative unfolding [28] or the maximum binned likelihood method [27,32].

[*]Deceased.
[†]Affiliated member at Kavli IPMU (WPI), University of Tokyo, Tokyo, Japan.
[‡]Also at National Research Nuclear University "MEPhI" and Moscow Institute of Physics and Technology, Moscow, Russia.
[§]Also at JINR, Dubna, Russia.
[‖]Present address: CERN, Geneva, Switzerland.
[¶]Also at J-PARC, Tokai, Japan.
[**]Also at BMCC/CUNY, Science Department, New York, New York, USA.
[††]Also at Nambu Yoichiro Institute of Theoretical and Experimental Physics (NITEP), Osaka City University, Osaka, Japan.

The analysis in this paper determines the kinematics of the outgoing μ^+ produced in $\bar{\nu}_\mu$ CC0π interactions on water. The differential cross sections are extracted by following a similar analysis procedure as that used in a previous T2K publication [32].

In the following sections, we describe the T2K anti-neutrino beam and near detector (ND280), the Monte Carlo simulation and data samples, the event selection, the cross section extraction method, the results, and model comparisons.

II. T2K EXPERIMENT

The T2K experiment [3] is a long-baseline neutrino experiment located in Japan. It is composed of a neutrino beam line and a near detector at the Japan Proton Accelerator Research Complex (J-PARC) laboratory in Tokai, and a far detector, Super Kamiokande (SK), that is situated 295 km away in the Mozumi Mine in the Kamioka area of Hida City. The J-PARC synchrotron produces a 30 GeV energy proton beam that strikes a graphite target to produce pions and kaons that are focused by three horn magnets into a 96 m long decay volume. The horn magnet polarity can be set to select either positively or negatively charged pions and kaons to produce a predominately neutrino or antineutrino beam. The magnet setting for positively and negatively charged tracks is denoted as forward horn current and reverse horn current (RHC), respectively. The near detector complex, 280 m downstream of the target, consists of an on-axis detector (INGRID) and an off-axis detector (ND280). The ND280 and SK detectors are positioned 2.5° away from the neutrino beam axis. At this angle, neutrino and antineutrino beams energies peak near 0.6 GeV. The following subsections describe the $\bar{\nu}_\mu$ beam, the ND280 detector, and the Monte Carlo simulation programs.

A. T2K BEAM

The neutrino and antineutrino fluxes for the RHC configuration in the ND280 detector were determined by simulating the T2K neutrino beam line [33] using the FLUKA2011 [34,35], GEANT3 [36], and GCALOR [37] software packages. The simulated hadronic yields have been reweighted using the NA61/SHINE [38–40] thin-target measurements and this reduced the flux uncertainties to be less than 10% around the flux peak. The $\bar{\nu}_\mu$ fluxes are plotted in Fig. 1 along with the three background neutrino flavors (ν_μ, ν_e, and $\bar{\nu}_e$). In the peak region (~0.6 GeV) the ν_μ contamination in the antineutrino flux is ~2.5%. Details on the antineutrino beam and comparisons to the neutrino beam have been discussed in a previous T2K publication [41].

B. ND280 DETECTOR

The ND280 detector consists of subdetectors inside the refurbished UA1/NOMAD magnet, which produces a 0.2 T magnetic field that is normal to the neutrino beam and the vertical direction. The ND280 subdetectors include the π^0 detector [42] (PØD), three tracking time projection chambers [43] (TPC1-3), two fine-grained detectors (FGD1-2) interleaved with TPC1-3, and an electromagnetic calorimeter (ECAL) that encloses the PØD, TPC1-3, and FGD1-2 subdetectors. For the analysis reported in this paper, the PØD and the TPC tracking detector in the ND280 detector complex are used. We define the $+z$ direction parallel to the neutrino beam direction and the $+y$ direction pointing vertically upwards.

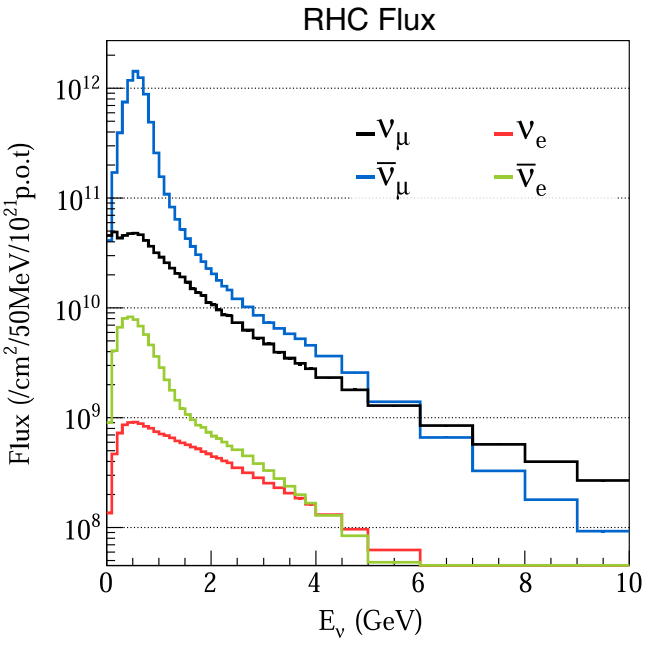

FIG. 1. The RHC flux given per cm^2/50 MeV/10^{21} PoT as a function of energy at the ND280 detector for the different neutrino components ($\bar{\nu}_\mu$, ν_μ, $\bar{\nu}_e$, ν_e).

We describe detector details relevant for the analysis. The PØD detector that reconstructs the neutrino interaction vertex is shown in Fig. 2. It contains 40 scintillator module planes (called PØDules), each consisting of two perpendicular arrays of triangular scintillator bars, 134 horizontal (x) bars, and 126 vertical (y) bars. Each bar has a wavelength shifting fiber centered in the bar that is read out by a Hamamatsu multipixel photon counter. P0Dules are formed into three major groups. The center group, called the water target, is the primary target for this analysis. It has 26 PØDules interleaved with 2.8 cm thick water bags and 1.3 mm thick brass sheets. The water target region is drainable and data can be taken with or without water. The fiducial volume mass is 1900 kg of water and 3570 kg of other materials. The two other regions (called upstream and central ECALs) are the upstream and downstream groups that each contain seven PØDules sandwiched with lead sheets clad with steel. These two groups form a veto region to isolate neutrino interactions that occur in the water target. The size of the entire active P0D volume is

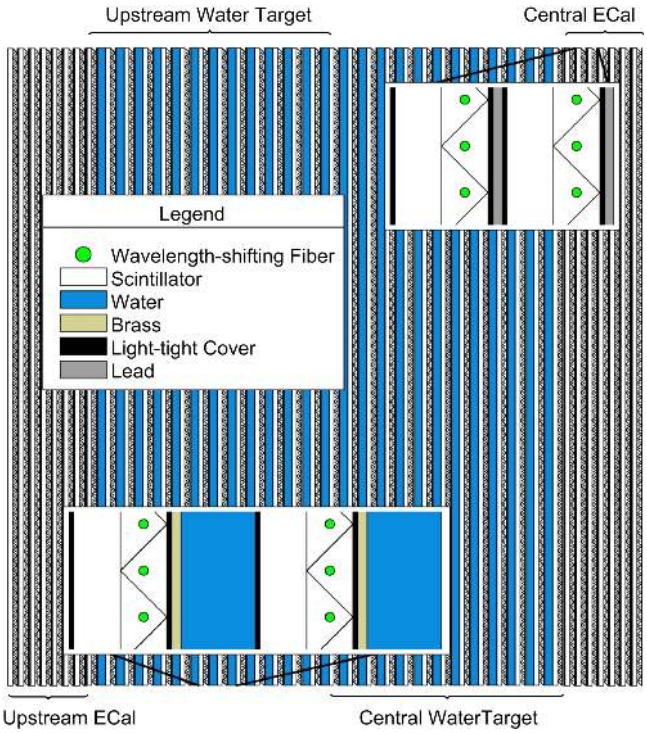

FIG. 2. Side view schematic diagram of the PØD detector. The white, zigzag, and blue regions represent the vertical scintillator bars, horizontal scintillator bars, and water bag regions, respectively. The vertical and horizontal bars represent an x-y module or PØDule. The first and last groups of seven PØDules form the upstream and central ECAL "super" modules, and the middle 26 PØDules interleaved with the water bags are the water target region. In this drawing, the beam direction ($+z$) is to the right, the $+y$ direction is up, and the $+x$ direction is into the figure.

$2103 \times 2239 \times 2400$ mm^3 (xyz) and its mass with and without water is 15 800 and 12 900 kg, respectively. The two other regions (called upstream and central ECALs) are the upstream and downstream groups that each contain seven PØDules and steel sheets clad with lead. These two groups form a veto region to isolate neutrino interactions that occur in the water target.

The charged-current neutrino interaction in the PØD creates a muon that exits the PØD and enters the TPC1-3 detectors. The TPC1-3 detectors measure the μ^+ momentum and its dE/dx energy loss which is used for muon particle identification.

III. DATA AND MONTE CARLO SAMPLES

The studies reported here used the RHC $\bar{\nu}_\mu$ beam running mode. The runs utilized detector configurations where the PØD water bags were filled (water-in) or empty (water-out). Roughly equal amounts of exposure in each configuration was allowed in each running period so that the detector operations, efficiencies, and beam conditions were similar for both the water-in and water-out data samples.

TABLE I. PoT for data and equivalent MC samples for RHC antineutrino beam running split for PØD water-in/water-out modes.

PØD target mode	Data sample	MC sample
Water-in	2.87×10^{20}	20.8×10^{20}
Water-out	3.43×10^{20}	20.9×10^{20}

A. Data samples

The total proton on target (PoT) exposure for RHC antineutrino beam data running is shown in Table I. This sample required all data quality cuts to be satisfied and corresponded to 2.87×10^{20} PoT for the water-in and 3.43×10^{20} PoT for the water-out modes.

B. Monte Carlo simulation

The analysis utilized simulated Monte Carlo (MC) samples with different beam and detector configurations for each data run. The total MC combined water-in and out samples were equivalent to 20.8×10^{20} and 20.9×10^{20} PoT, respectively. The simulation includes the following:

(1) Primary $\bar{\nu}_\mu$ and background ν_μ, ν_e, and $\bar{\nu}_e$ beam production in the graphite target and propagation through the following horns and decay volume. The hadronic rates from the beam target were generated by FLUKA2011 which was tuned to the NA61/SHINE measurements, and the GEANT3 simulation software predicted the flux and energy spectrum for the different neutrino flavors.

(2) The antineutrino and neutrino interactions in the ND280 detector, where the NEUT [44] MC generator (v5.3.3) is used to calculate the interaction cross sections and the final-state particle kinematics.

(3) The detector response used the GEANT4 [45] simulation package (v4.9.4.p04) with its physics list [46] to transport the final-state particles through the ND280 detector complex.

IV. EVENT AND KINEMATIC SELECTION

The event selection for antineutrino interactions is optimized to identify the observable charged-current events with no charged or neutral pions in the final state. This is nominally denoted as the CC-0π final state. This mainly includes charged-current quasielastic (CCQE) events and the case where pions are created in the primary resonant antineutrino interaction, but reabsorbed before exiting the nucleus. The $\bar{\nu}_\mu$ interactions with a multinucleon state such as a two-particle two-hole (2p2h) state can produce a final state without mesons. Non-CCQE neutrino interactions that produce a CC-0π final state will have antineutrino kinematics that are different from those created in CCQE interactions. This will be important to understand and to carefully model since this can change the antineutrino

energy reconstruction which can affect current and future neutrino oscillation analyses.

We first consider three antineutrino mode selections (CC-inc, CC-0π, and CC-1π). The event selection is similar to a previous T2K analysis [28] of a neutrino differential cross section measurement on water in the PØD detector. The selection requires the following:

(1) Overall ND280 data quality flags are good such that the detector was operational and stable during taking data. There is at least one track reconstructed in TPC1 and there is a reconstructed track in the PØD that matches a track in the TPC with the start of the track reconstructed in the fiducial volume of the PØD water target.
(2) There is a muon track candidate that is the highest-momentum positively charged track, the highest-momentum track in the event, and has a TPC dE/dx track measurement consistent with a muon energy loss. These first four requirements define the CC-Inc event selection.
(3) There are no reconstructed PØD showers in the event. This cut removes charged-current events with a π^0.
(4) Remaining events are then separated into three categories based on the number of μ-like PØD tracks in the event.
    (a) Events with only a muon track candidate define the CC-0π selection.
    (b) Events with a muon track candidate and one μ-like track define the CC-1π selection.
    (c) All other remaining events are not selected.

If there are other tracks besides the muon track candidate, they are defined as μ-like if the average energy loss per PØD layer near the middle of the track is less than 1.5 times that of the muon track candidate in the same event. The μ^+ track candidate is a minimum ionizing particle track which should have nearly the same measured energy loss per unit length of the pion track as measured in between the interaction vertex and before it decays in the detector. Comparing the average energy losses between the muon track candidate and different PØD tracks in the same event ensures that the tracks use the same detector gain calibrations. Using this cut, proton and pion tracks can be differentiated, allowing for any number of protons to be present in CC-0π events.

In Table II, the purity and efficiency of the three selections (columns 2–4) are given in terms of five true MC final states (column 1). The true final states are CC-0π, CC-1π, CC-other (all other CC states excluding CC-0π and CC-1π), BKGD (neutral-current and non-$\bar{\nu}_\mu$ interactions) and OOFV (out-of-fiducial-volume events). The OOFV events have interactions that occur outside the selected PØD target region. This table shows that the CC-0π selection has very good purity ($\sim$80%) and very high efficiency ($\sim$95%) relative to the CC-Inc sample.

TABLE II. Purity and efficiency tables for the different selections for water-in and water-out samples. The true final states are given in the first column and the three selections (CC-Inc, CC-0π, and CC-1π) are given in the rows below the double lines. An example in this table is that the water-out mode CC-0π selected sample will have 82% of its events originate from the true CC-0π final state. The $\epsilon_{\text{relative}}$ is the fraction of relevant events (CC-0π or CC-1π) present in the CC-Inc sample retained by the number of μ-like tracks requirement. For example, 96% of the CC-0π events present in the water-in CC-Inc sample are retained in the water-in CC-0π sample. See text for final-state descriptions.

	% in selected sample		
Water-in mode:	CC-Inc	CC-0π	CC-1π
CC-0π	60	80	10
CC-1π	17	13	57
CC-Other	13	3	15
BKGD	7	1	15
OOFV	4	2	3
$\epsilon_{\text{relative}}$		96	14

	% in selected sample		
Water-out mode:	CC-Inc	CC-0π	CC-1π
CC-0π	58	82	11
CC-1π	16	12	57
CC-other	12	2	14
BKGD	8	1	14
OOFV	5	2	4
$\epsilon_{\text{relative}}$		95	15

In Fig. 3 we plot the CC-0π and CC-1π selections of data superimposed over the NEUT simulations. This is presented in pairs of water-in/-out samples for the CC-0π momentum, CC-0π cosθ, CC-1π momentum, and CC-1π cosθ. The Monte Carlo color bands correspond to the true CC-0π, CC-1π, CC-Other, BKGD, and OOFV events. Overall, there is reasonable agreement between data and Monte Carlo.

In Table II and Figs. 3(a)–3(d), the dominant backgrounds for the CC-0π selection are caused by misidentified CC events with one emitted pion (CC-1π) or CC-other events, with CC-1π being the largest of the two. In order to constrain the CC-1π background, a control sample of CC-1π selected events will be included in the analysis fitting described in the next section. This allows a data constraint on the background estimation, which leads to smaller background modeling uncertainties.

V. DOUBLE-DIFFERENTIAL CROSS SECTION FITTING METHOD

In this section we first describe the fitting and unfolding technique to extract the differential cross section in true $p - \cos\theta$ bins of the μ^+ track. Then the binning choice is explained, followed by descriptions of the fit parameters

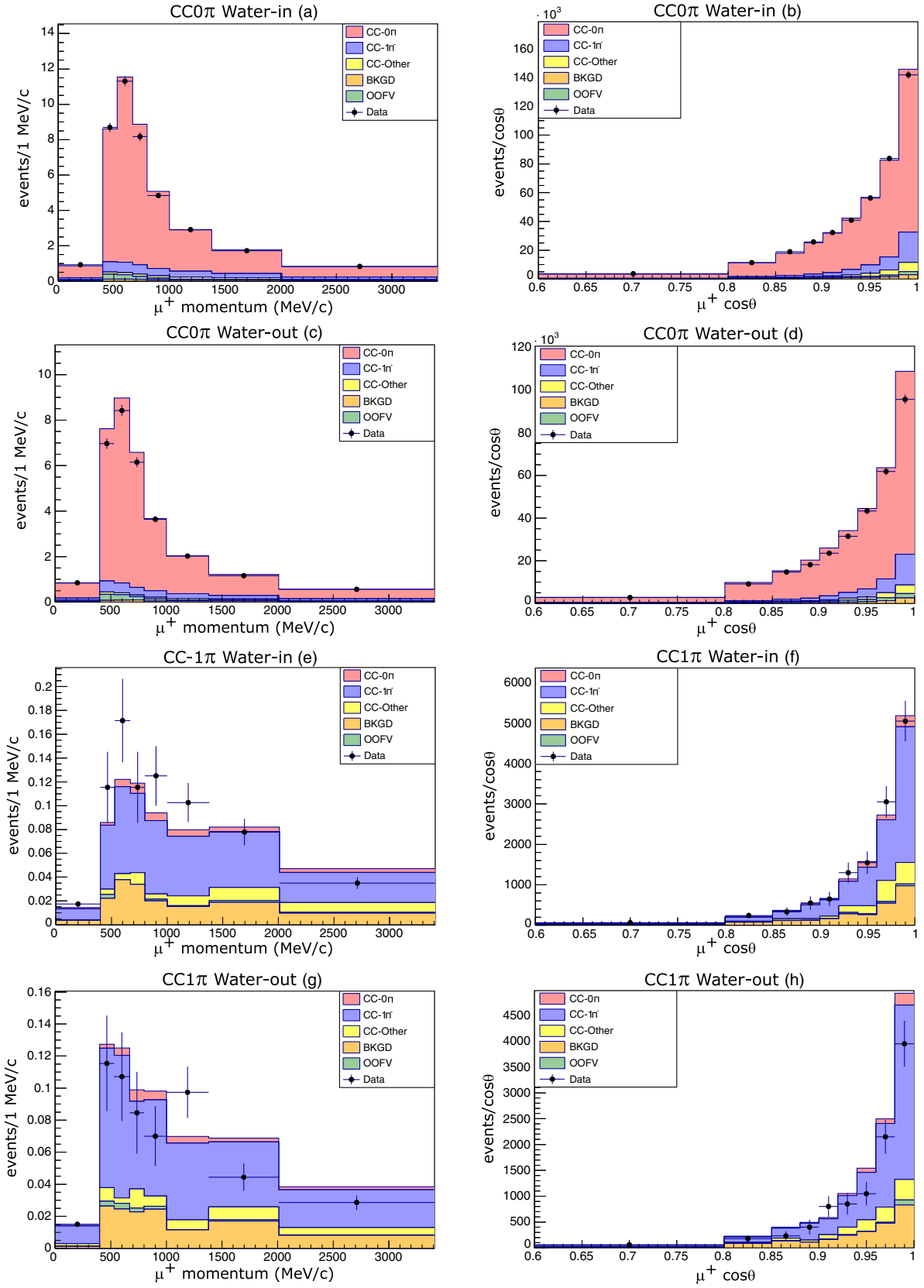

FIG. 3. Comparisons of lab-frame momentum (left column) and cos θ (right column) distributions between data (black dots with error bars) and NEUT simulation predictions before fitting (stacked color bands). The CC-0π selections have been applied on the water-in samples [(a) and (b)] and water-out samples [(c) and (d)]. The CC-1π selections have been applied on the water-in samples [(e) and (f)] and water-out samples [(g) and (h)].

and checks and validation of the fitting method. Finally, the regularization choice and overall checks are discussed.

A. Fitting

In an idealized experiment with no backgrounds and perfect detector resolutions, the differential cross section as a function of the kinematic variable x in a particular bin j is denoted as Δx_j and the cross section is given as

$$\frac{d\sigma}{dx_j} = \frac{N_j}{\epsilon_j \Phi T \Delta x_j}, \tag{1}$$

where N_j is the number of measured events in bin j, T is the number of target nuclei, Φ is the neutrino flux per unit area, and ϵ_j is the efficiency to reconstruct a signal event in bin j. In this analysis, the differential area Δx_j is the $p-\cos\theta$ bin of the μ^+ track in the lab frame. We define N_j^{sig} as the number of signal events and $N_j^{\text{sig,MC}}$ as the number of predicted MC events in $p-\cos\theta$ bin j. We introduce a scale parameter c_j to be fitted, where

$$N_j^{\text{sig}} = c_j N_j^{\text{sig,MC}}. \tag{2}$$

If we include different background types k in the reconstructed data, $\sum_k^{\text{bkgd types}} N_j^{\text{bkgd}\,k,\text{MC}}$ should be added to the above equation. In addition, if the background event rates depend on different model parameters, the backgrounds can be reweighted by a product term $\prod_a^{\text{model}} \omega(\vec{a})_j^k$, which depends on a vector $\vec{a}$ of background model parameters. Then, the expression becomes

$$N_j = c_j N_j^{\text{sig,MC}} + \sum_k^{\text{bkgd types}} \left(\prod_a^{\text{model}} \omega(\vec{a})_j^k \right) N_j^{\text{bkgd}\,k,\text{MC}}, \tag{3}$$

where N_j is the predicted number of measured events (signal + background) in bin j, c_j are the fitted parameters and $\vec{a}$ is the vector parameter.

In real experiments the reconstruction is not perfect and we need to allow for smearing where events from a particular true $p-\cos\theta$ bin j were smeared over several different reconstructed $p-\cos\theta$ bins. If we consider events in some true kinematic bin j that are reconstructed with kinematics across bins indexed by i, a "smearing matrix" S_{ij} can be constructed:

$$S_{ij} = \frac{N_{\text{reco in}\,i}^{\text{true in}\,j}}{N^{\text{true in}\,j}}, \tag{4}$$

where $N_{\text{reco in}\,i}^{\text{true in}\,j}$ is the number of events reconstructed in bin i that had true kinematics corresponding to bin j, and $N^{\text{true in}\,j}$ is the number of events with true kinematics corresponding to bin j. The equation for the predicted observed number of events N_i in terms of the events in true kinematic bin j becomes

$$N_i = \sum_j^{N_{\text{bin}}} S_{ij} \Bigg\{ c_j N_j^{\text{sig,MC}} + \sum_k^{\text{bkgd types}} \left(\prod_a^{\text{model}} \omega(\vec{a})_j^k \right) N_j^{\text{bkgd}\,k,\text{MC}} \Bigg\}. \tag{5}$$

Equation (5) forms a mapping between true bin j and reconstructed bin i. This approach [32] after fitting the parameters will *unfold* the true number of events $c_j N_j^{\text{sig,MC}}$ in bin j from the observed data. Using the histogram of observed reconstructed events N_i^{obs} and the predicted number of observed events $N_i(\vec{c},\vec{a})$ from Eq. (5), which depends on the fit parameters c_j and model parameters $\vec{a}$, we can form the binned likelihood of a histogram [47] as

$$-2\ln(L)_{\text{stat}} = \sum_i^{\text{bins}} 2 \Bigg\{ N_i(\vec{c},\vec{a}) - N_i^{\text{obs}} + N_i^{\text{obs}} \ln\left(\frac{N_i^{\text{obs}}}{N_i(\vec{c},\vec{a})} \right) \Bigg\}, \tag{6}$$

which will be minimized.

In addition, three penalty terms are added to Eq. (6). The first is

$$-2\ln(L)_{\text{bkgd}} = (\vec{a}-\vec{a}_{\text{prior}})^T [V_{\text{cov}}^{\text{model}}]^{-1} (\vec{a}-\vec{a}_{\text{prior}}), \tag{7}$$

where $V_{\text{cov}}^{\text{model}}$ is a covariance matrix containing the uncertainties and correlated errors on the background model parameters $\vec{a}$ and the initial parameter value is given as $\vec{a}_{\text{prior}}$, which has been discussed in Ref. [41].

The number of observed events includes a flux term that is the number of $\bar{\nu}_\mu$ per unit area. This term has been modeled for the different neutrino energies as $\sum_n^{E_\nu} f_n^i$, where f_n^i is the fraction of antineutrinos in flux energy bin n for reconstructed bin i. This nominally sums to unity. The flux uncertainty is given in a covariance matrix $V_{\text{cov}}^{\text{flux}}$ and this adds to Eq. (6) the flux penalty term

$$-2\ln(L)_{\text{flux}} = (\vec{f}-\vec{f}_{\text{prior}})^T [V_{\text{cov}}^{\text{flux}}]^{-1} (\vec{f}-\vec{f}_{\text{prior}}). \tag{8}$$

Finally, the detector systematic uncertainties are given in a third covariance matrix $V_{\text{cov}}^{\text{det}}$, with $\vec{r}$ parameters which vary the reconstructed event rate r_i in bin i. This adds the last penalty term, given as

$$-2\ln(L)_{\text{det}} = (\vec{r}-\vec{r}_{\text{prior}})^T [V_{\text{cov}}^{\text{det}}]^{-1} (\vec{r}-\vec{r}_{\text{prior}}). \tag{9}$$

The measurement described here is concerned with events that occur specifically on water targets. The number of signal events occurring on water and non-water targets are

allowed to vary independently in the fit so that the interaction rate on only water targets can be extracted. We introduce a second set of scaling parameters d_j for events that occur on non-water targets:

$$N_i = r_i\left(\sum_n^{E_\nu} f_n^i\right)\sum_j^{N_{\rm bin}} S_{ij}\left\{c_j N_j^{\rm sig,water,MC} + d_j N_j^{\rm sig,non\text{-}water,MC} + \sum_k^{\rm bkgd\_types}\left(\prod_a^{\rm model}\omega(\vec{a})_j^k\right)N_j^{{\rm bkgd}\_k,{\rm MC}}\right\}. \quad (10)$$

Data samples where there was no water in the PØD bags serve to constrain the d_j parameters so that while simultaneously fitting water-in and water-out data, the unfolded CC-0π event rate on water is extracted from the data as the $c_j N_j^{\rm sig,water,MC}$ term.

The final log-likelihood equation of all terms that will be minimized to fit the data is

$$-2\ln(L)_{\rm tot} = -2ln(L[\vec{c},\vec{d},\vec{a},\vec{f},\vec{r}])_{\rm stat} - 2\ln(L[\vec{a}])_{\rm bkgd} - 2\ln(L[\vec{f}])_{\rm flux} - 2\ln(L([\vec{r}]))_{\rm det}, \quad (11)$$

where the fit-parameter dependence of each likelihood term is made explicit. Note that, ultimately, we are interested in the $\vec{c}$ fit parameters that will be used to extract the unfolded true differential water cross section. This method differs from the D'Agostini iterative unfolding method used in Ref. [28], which used a single iteration and did not compare results with and without regularization.

B. Binning choice

The choice of the two-dimensional (2D) μ^+ track $p-\cos\theta$ binning was determined by the following considerations:

(1) The number of events in each 2D bin should have reasonable statistics, ~100 events. This improves the stability of the fit results.
(2) The selection efficiency should be relatively high to minimize model dependence of the efficiency correction, and event populations should not differ very much between adjacent bins which also improves the stability of the fit results.
(3) The bin sizes should be fine enough that local detector resolution effects are well represented and the detector resolutions do not change too much from bin to bin, but not too fine such that there are too few events in the bin.

We expect that these choices should reduce regularization complications (which are discussed in later sections), or possibly even the need for regularization. The 28 bins over the entire kinematic phase space are specified in Table III. The 2D plot in Fig. 4 contains the efficiencies of the water-in (a) and water-out (b) data sets.

TABLE III. The $p-\cos\theta$ bins over all kinematic phase space.

Bin index	True momentum MeV/c	True $\cos\theta$ Bin edge
1	0–400	−1, 1
2–4	400–530	−1, 0.84, 0.94, 1
5–8	530–670	−1, 0.85, 0.92, 0.96, 1
9–12	670–800	−1, 0.88, 0.93, 0.97, 1
13–16	800–1000	−1, 0.90, 0.94, 0.97, 1
17–20	1000–1380	−1, 0.91, 0.95, 0.97, 1
21–24	1380–2010	−1, 0.92, 0.96, 0.98, 1
25–27	2010–3410	−1, 0.95, 0.98, 1
28	3410–50 000	−1, 1

Among the 28 bins covering the entire kinematic region, there are bins that have very few events due to the phase space or due to the low detector efficiency. These include the first ($p < 400$ MeV/c) and last ($p > 3410$ MeV/c) bins and lowest-lying $\cos\theta$ bins in each of the seven given momentum slices in the middle momentum ($400 < p < 3410$ MeV/c) bins. Although we will fit in all 28 bins, we do not use these nine bins in the final differential cross section determinations. Instead, we use the other 19 bins for the final differential cross section measurements. These 19 cross section bins are given in Table IV and their index number is called a cross section bin.

C. Fit parameters, systematic errors, and checks

The five types of parameters in the likelihood fit in Eq. (11) include; $\vec{c}$ (signal interaction parameters on water targets), $\vec{d}$ (signal interaction parameters on non-water targets), $\vec{f}$ (fractional flux parameters), $\vec{a}$ (background model parameters), and $\vec{r}$ (reconstruction event rate scale factors). All parameter types are listed with their numbers in Table V. We describe each parameter type in the following paragraphs.

There are two sets of 28 scale factors for the $p-\cos\theta$ bins: one set $\vec{c}$ for interaction on water and another set $\vec{d}$ for non-water interactions. The water parameters $\vec{c}$ contain the subset of 19 parameters that are used to extract the final unfolded cross section.

There are 11 flux parameters representing the fraction of the $\bar{\nu}_\mu$ flux in varying energy bin widths with energy boundaries at 0, 0.4, 0.5, 0.6, 0.7, 1.0, 1.5, 2.5, 3.5, 5.0, 7.0, and 30.0 GeV. The pre-fit flux uncertainties are on the order of ~10% in the matrix $V_{\rm cov}^{\rm flux}$.

There are nine background model parameters and six pion final-state interaction (FSI) parameters. The first three background model parameters—the axial mass, axial form factor, and fraction of nonresonant background—describe the main background, which is the charged-current resonant background. The charged-current deep inelastic background is described using a scaling parameter on a normalization function of the cross section, which depends on the neutrino energy. The other background model parameters are normalization rates for the charged-current coherent interactions on carbon and oxygen,

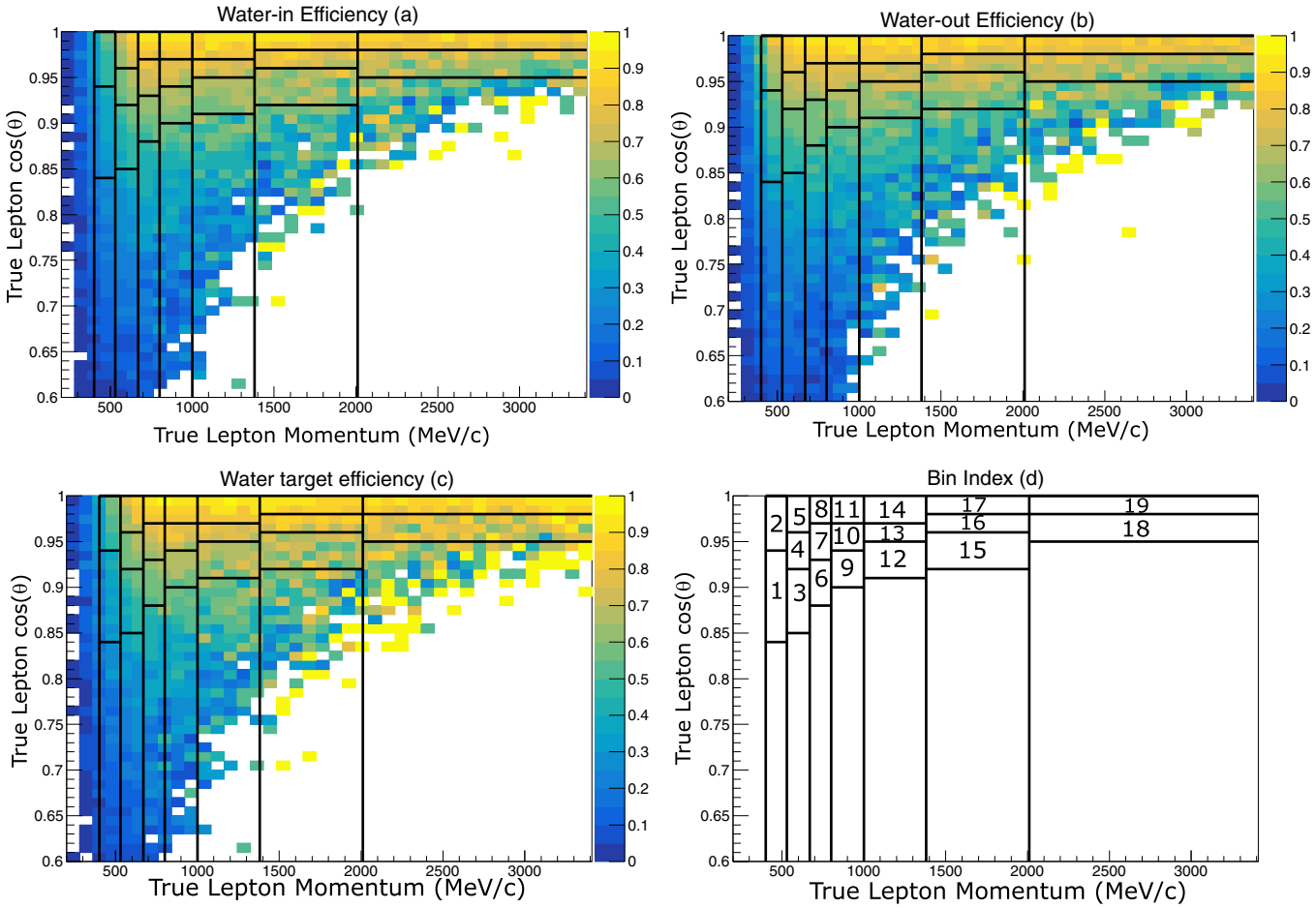

FIG. 4. The CC-0π selection efficiency plots in 2D p vs $\cos\theta$ bins for water-in (a), water-out (b), and water target only (c). There are 28 bins whose edges are drawn with vertical and horizontal lines. The efficiencies are given in color bands and it is noted that the efficiencies are very similar. The last plot (d) is the bin index given in Table IV. Note that the twenty-eighth bin in Table III is outside the plot boundary. The fit results in Sec. VI A use these 19 bins, which are a subset of the 28 bins.

neutral-current, and coherent neutral-current backgrounds. The nominal values and their uncertainties for signal, background, and FSI parameters in the fit are given in Table VI. More details about those parameters can be found in Ref. [48].

The six pion FSI parameters include effects for absorption, production, charge exchange, and quasielastic scattering inside the nucleus. For descriptions of these FSI parameters see Table IV in the previous T2K publication [49].

TABLE IV. The $p-\cos\theta$ bins used for the unfolded cross sections and indexed as cross section bin numbers.

Bin index	Momentum MeV/c	$\cos\theta$ Bin edge
1, 2	400–530	0.84, 0.94, 1
3, 4, 5	530–670	0.85, 0.92, 0.96, 1
6, 7, 8	670–800	0.88, 0.93, 0.97, 1
9, 10, 11	800–1000	0.90, 0.94, 0.97, 1
12, 13, 14	1000–1380	0.91, 0.95, 0.97, 1
15, 16, 17	1380–2010	0.92, 0.96, 0.98, 1
18, 19	2010–3410	0.95, 0.98, 1

The efficiency dependence on the signal CC-0π model parameters was also included. As already mentioned, the signal is almost entirely made up of interactions from CCQE, 2p2h, and resonant pion production with a subsequent pion absorption FSI. The uncertainty on the neutrino-nucleon aspect of CCQE interactions is considered through variations of the nucleon axial mass, while the nuclear aspect of the interactions is considered through variations of the nuclear ground-state model (the Fermi motion and removal energy), very similarly to that described in Ref. [41] (to remain conservative the size

TABLE V. Table of parameters in the fit.

Symbol	Parameter	Number
$\vec{c}$	Signal on water coefficients	28
$\vec{d}$	Signal on non-water coefficients	28
$\vec{f}$	Flux parameters	11
$\vec{r}$	Detector parameters	76
$\vec{a}$	Background and FSI parameters	15

TABLE VI. List of nominal values and uncertainties of six signal model, nine background, and six FSI parameters used in the fitting. Note that $p_0 = 500$ MeV/c.

Parameter	Nominal value	Uncertainties (1σ)
CCQE-like		
M_A^{QE}	1.15 GeV/c^2	0.41 GeV/c^2
p_F ^{12}**C**	223 MeV/c	31 MeV/c
p_F ^{12}**O**	225 MeV/c	31 MeV/c
E_b ^{12}**C**	25 MeV/c	9 MeV/c
E_b ^{16}**O**	25 MeV/c	9 MeV/c
2p2h normalization ^{12}**C**	1	1
2p2h normalization ^{16}**O**	1	1
1π		
C_{A5}	1.01	0.12
M_A^{RES}	0.95 GeV/c^2	0.15 GeV/c^2
Isospin 1/2 bg	1.3	0.2
CC multipion and DIS production	0	0.4
CC coherent normalizations		
CC coherent ^{12}**C**	1	1
CC coherent ^{16}**O**	1	1
NC interactions normalizations		
NC coherent	1	0.3
NC multipion and DIS production	1	0.3
Secondary pion interaction normalizations		
Pion absorption	1	0.41
Pion charge exchange ($p_\pi < p_0$)	1	0.57
Pion charge exchange ($p_\pi > p_0$)	1	0.28
Pion quasielastic ($p_\pi > p_0$)	1	0.41
Pion quasielastic ($p_\pi < p_0$)	1	0.34
Pion production	1	0.5

of the uncertainty is slightly increased, as indicated in Table VI). The uncertainties on 2p2h interactions are treated as normalization parameters, with 100% uncertainty. In all of these nuclear uncertainties carbon and oxygen interactions are not considered to be fully correlated. All of the signal model parameters are varied to calculate the efficiency uncertainty but are not included in the fitter as nuisance parameters.

The detector parameters $\vec{r}$ scale the predicted number of reconstructed events in Eq. (10) in each bin i of reconstructed μ^+ kinematics. These parameters are also included in the penalty terms in Eq. (9) and, being scale factors, they are nominally set to 1.0. There is one parameter for each of the 19 cross section bins for each water-in/water-out sample of the CC-0π and CC-1π selections. In total there are 76 detector parameters. The uncertainties of these parameters are determined from detector uncertainties in the TPC and the PØD detectors. The TPC and PØD momentum resolution and scale errors and the B-field distortions are estimated by varying their scales, resulting in a combined error of roughly 6%. The TPC charge misidentification, track reconstruction efficiency, shower reconstruction efficiency, and TPC-PØD matching errors are obtained by reweighting the parameters, resulting in a combined error of roughly 2.5%.

The remaining errors are due to the uncertainty on the mass of the non-water material in the PØD detector [28] (which was estimated to be 1.5%) and the mass of water in the filled water target bags. The uncertainty of the water mass in each PØD water bag was modeled by an uncorrelated normal distribution with a 10% standard deviation. The typical initial errors on the parameters representing the CC-0π samples are 5–10%, whereas the errors on the CC-1π samples are 10–20%.

Basic validation checks—that the fit behaves properly under the conditions that the MC matches the data with well defined conditions—were performed. The first check consisted of fitting the NEUT MC model to verify that all of the fitted water coefficients (c_j) and non-water coefficients (d_j) are exactly reproduced. The next check was to decrease/increase the water/non-water target masses by $\pm 50\%$ and check that the c_j and d_j parameters decrease/increase by the correct amount.

The systematic errors on the flux, background parameters, and detector systematics, which appear in the penalty terms in Eqs. (7)–(9), were checked by removing two of the three groups of nuisance parameters and checking the values of the refit water-in coefficients. When each of these groups is turned on and off one by one, we find that water-in coefficients have errors in the range of 2–6%, 2–6%, and 6–14% due to uncertainties on the flux, background models, and detector systematics, respectively.

Finally, five different samples of the NEUT MC model, with the same number of events as the expected data sample, were generated and fitted. The resulting water coefficients c_j were all consistent between all five samples. To evaluate how well the post-fit results agree with a certain prediction, we define the χ^2 between some prediction with label A and the post-fit results to be

$$\chi^2_A = (\vec{\sigma}_A - \vec{\sigma}_{\text{post-fit}})^T [V_{\text{cov}}^{\text{post-fit}}]^{-1} (\vec{\sigma}_A - \vec{\sigma}_{\text{post-fit}}). \quad (12)$$

The resulting χ^2's between the MC true event rates and the fitted ones from the five different samples had similar values.

D. Regularization

The aim of the analysis is to extract the parameters c_j which are proportional to the number of CC-0π events on water in the $p - \cos\theta$ bins for $i = 1, \ldots, 28$. This is obtained by fitting the parameters c_j in Eq. (10) which determines the predicted N_i that is used in the binned likelihood in Eqs. (6) and (11). This forms an inverse problem where small statistical fluctuations in the reconstructed event rates N_i can cause large variations of the fitted parameters c_j. Figure 5(a) shows the covariance matrix of the fitted parameters c_j using a MC simulation test sample. There are some moderate

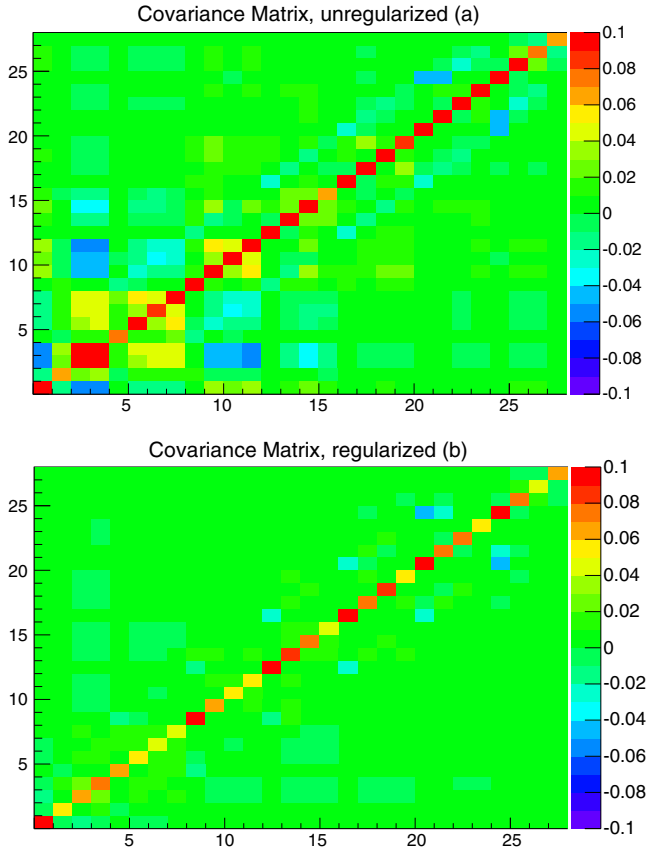

FIG. 5. Covariance matrix of water-in coefficients before (a) and after (b) regularization was applied to a test MC sample. The regularization reduces off-diagonal correlations.

bin-to-bin correlations seen in this covariance matrix. Specifically, there are off-diagonal anticorrelations between neighboring momentum bins for equivalent $\cos\theta$ bins. These are caused by the fit being able to adjust the event rates in neighboring true bins in an anticorrelated way and getting similar predictions in the reconstructed bins.

These bin-to-bin variations can be reduced by applying data-driven regularization methods, as discussed and applied in Sec. IV D of the previous T2K analysis [32]. The regularization technique [50] consists of adding to Eq. (11) an additional penalty term:

$$-2\log(L[\vec{c}, p_{\text{reg}}])_{\text{reg}} = p_{\text{reg}} \sum_{i}^{N_{\text{bin}}-1} (c_i - c_{\hat{i}})^2, \quad (13)$$

where $\hat{i}$ is the index of the bin corresponding to a neighboring momentum bin i for equivalent $\cos\theta$ bins. Equation (13) includes a parameter p_{reg} that controls the regularization strength between momentum bin boundaries. When Eq. (13) is added to Eq. (11) and the sum is minimized, this will clearly reduce variations between adjacent momentum bins depending on the size of p_{reg}. The L-curve regularization [51] is obtained when the ratio $-2\log(L[\vec{c}, p_{\text{reg}}])_{\text{reg}}/p_{\text{reg}}$ has the largest curvature as a function of p_{reg} [51]. The p_{reg} values of 1–2 were found to have the largest curvature in this test sample, as shown in Fig. 5(a). When regularization with $p_{\text{reg}} = 1$ is applied to the test sample, the off-diagonal covariances and the bin-to-bin correlations are reduced, as shown in Fig. 5(b).

Both unregularized and regularized results will be shown. The regularized results will minimize unphysical large bin-to-bin fluctuations. We note that regularization can potentially bias signal model results. However, if unregularized and regularized results produce the same fit results, the signal model results are the same and unbiased.

The purpose here is to provide, at the same time, fully correct and model-independent results (unregularized) which are properly interpreted together with a full covariance matrix provided in a data release.

VI. DATA RESULTS AND COMPARISON TO MODELS

A. Fit results

The unregularized and regularized fit results of event rates with errors for the 19 bins of the water CC-0π cross

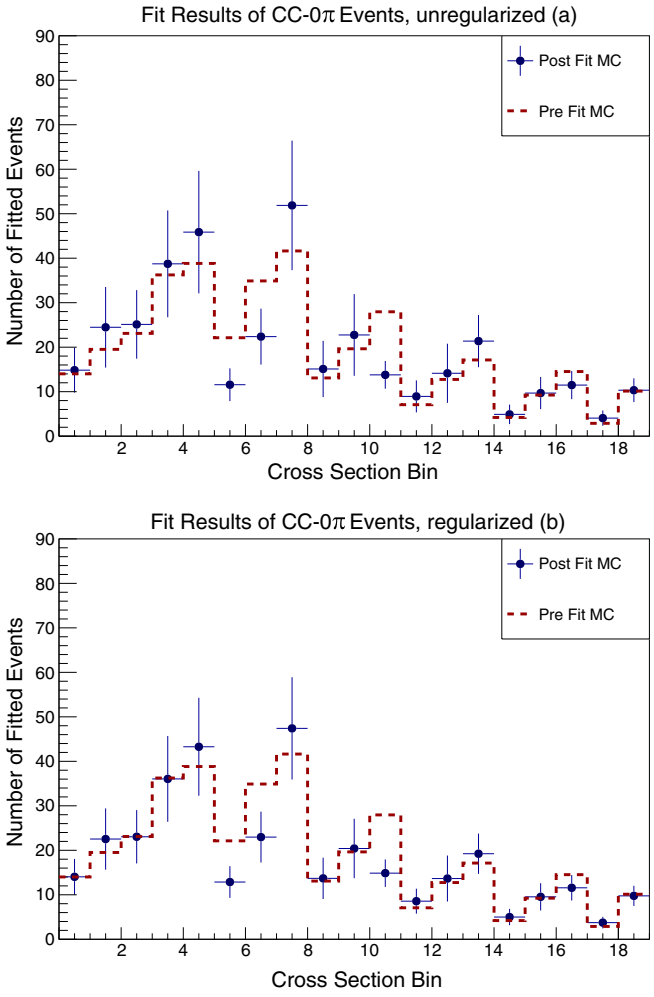

FIG. 6. Fit results of CC-0π events rates in 19 cross section bins for unregularized (a) and regularized (b) results for water events.

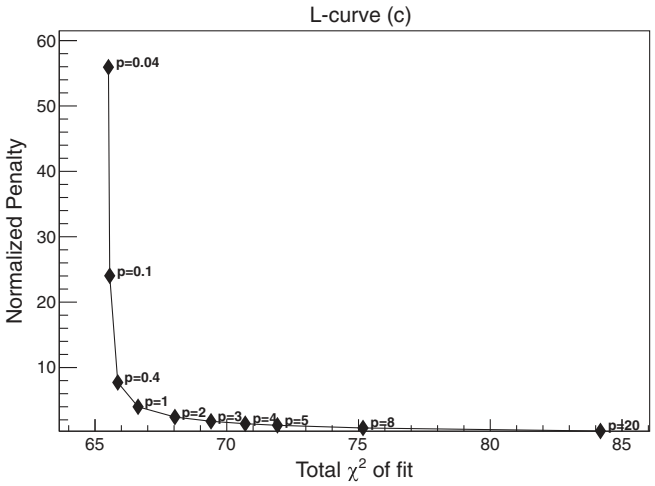

FIG. 7. Regularization L-curve of data for regularized results. Figure 6(b) is obtained when $p_{\text{reg}} = 1$.

section by cross section bin number are shown in Figs. 6(a) and 6(b), respectively. The unregularized and regularized fit results agree with each other to within a few tenths of one sigma. The L-curve of the regularized fits is shown in Fig. 7. The largest L-curvature occurs in data at 1, and we choose $p_{\text{reg}} = 1$ for the regularization.

The resulting fitted or post-fit results for the 28 water c_j and 28 non-water d_j parameters are shown in Figs. 8(a) and 8(b), respectively. The unregularized fit is in green and the regularized fit is in blue. The nominal initial values are set to 1.0, so the shifts or deviations from initial to post-fit values can be readily inspected. The post-fit c_j are centered on ~1 except for three (sixth, seventh, and eleventh) bins. We note that the non-water d_j parameters are centered on ~0.9; however, those same three bins in the post-fit non-water parameters do not have dips relative to their adjacent bins.

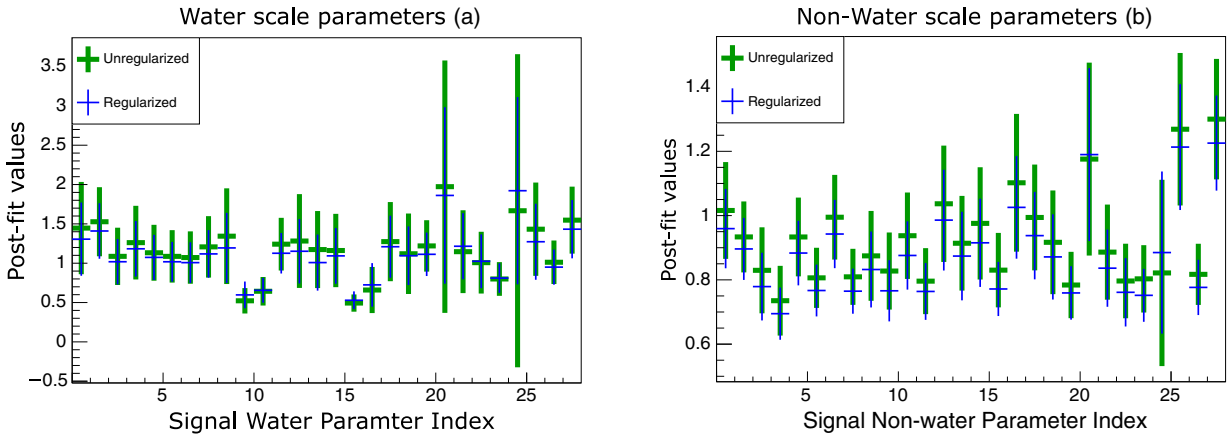

FIG. 8. Post-fit results of water (a) and non-water (b) events which correspond to the 28 scale parameters c_j and d_j, respectively.

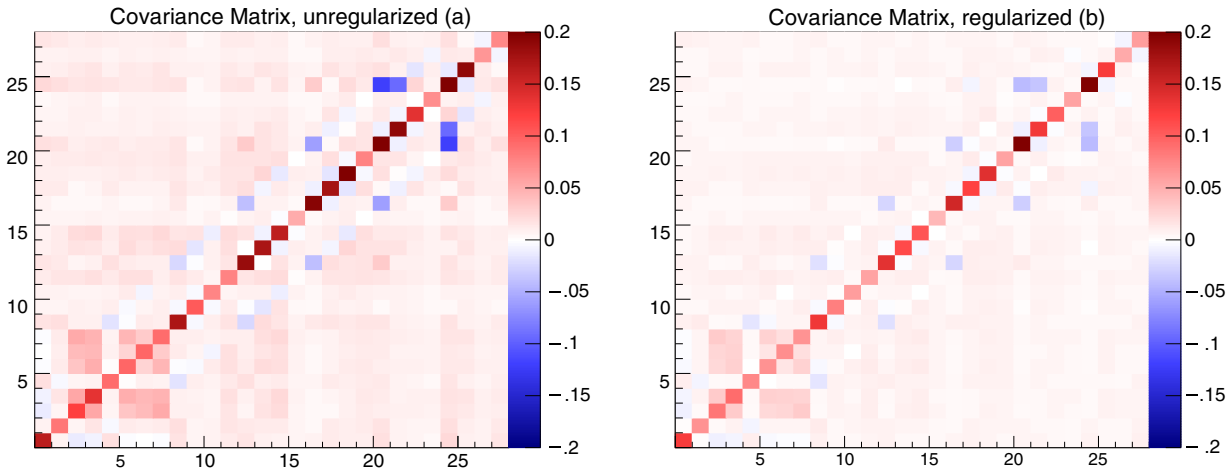

FIG. 9. Covariance matrix of water parameters for unregularized fits (a) and regularized fits (b).

The covariance matrix of the fit results of the water c_j parameters are shown in Figs. 9(a) and 9(b) for unregularized and regularized fits, respectively. In the unregularized covariance we observe slight positive (red bins) covariance correlations at low momentum ($p < .67$ GeV/c) and a negative (blue bins) correlation in bin 25, which is a high-momentum ($p > 2.01$ GeV/c) bin.

B. Cross section comparisons to NEUT and other models

The regularized and unregularized fit results of unfolded p vs $\cos\theta$ bins of data (black crosses) with comparisons to cross section predictions from NEUT (v5.41), GENIE (v2.12.10), and NuWro (v18.02.1) models are shown in Figs. 10 and 11, respectively.

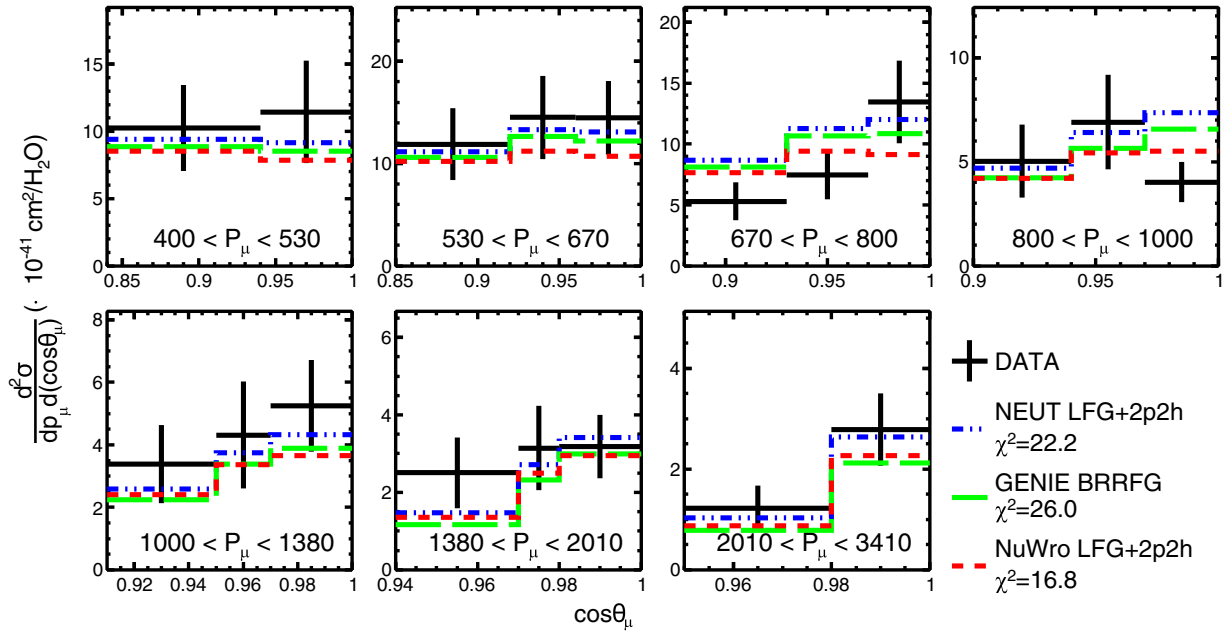

FIG. 10. Regularized fit results of data as a function of 19 $\cos\theta$ bins in seven different momentum ranges with comparisons to NEUT (v5.41), GENIE (v2.12.10), and NuWro (v18.02.1) predictions. The fit χ^2 of each model is defined by Eq. (13).

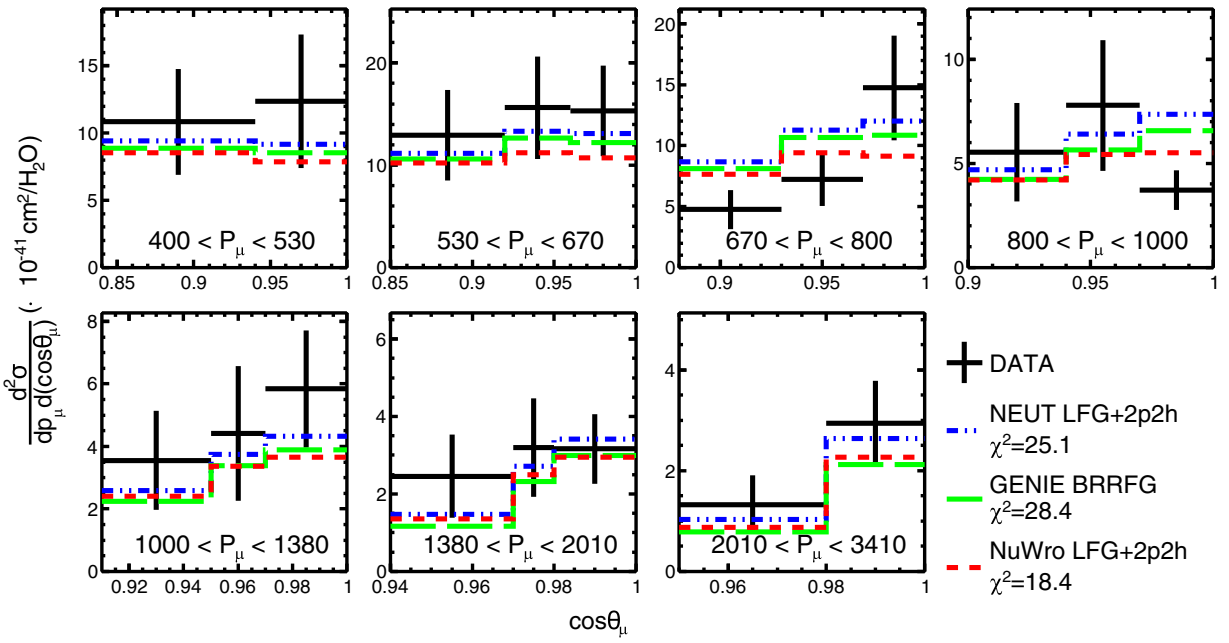

FIG. 11. Unregularized fit results on data as a function of 19 $\cos\theta$ bins in seven different momentum ranges with comparisons to NEUT (v5.41), GENIE (v2.12.10), and NuWro (v18.02.1) predictions. The fit χ^2 of each model is defined by Eq. (13).

TABLE VII. Comparison of the data results in both the regularized and unregularized cases to NEUT, GENIE, and NuWro using the absolute χ^2 from Eq. (12).

Generator	Data χ^2 (regularized)	Data χ^2 (unregularized)
NEUT	29.2	33.1
GENIE	26.0	28.4
NuWro	16.8	18.4

The NEUT and NuWro models both include local Fermi gas modeling with 2p2h effects and the GENIE model includes the Bodek-Richie modifications to the relativistic Fermi gas effects. These models have been described in a previous T2K publication [32] and the models were implemented using the NUISANCE framework [52]. The results are presented in seven plots of $\cos\theta$ bins in seven different momentum ranges from 0.4 to 3.41 GeV/c. The data mostly agrees within 1 standard deviation of all three predictions, except for the sixth, seventh, and eleventh data bins which are ∼2 standard deviations below the NEUT prediction. These correspond to the three low bins 6, 7, and 11 in Fig. 6, bins 10, 11, and 16 in Fig. 8, and the $670 < p < 800$ MeV/c (first and second) bins and $800 < p < 1000$ MeV/c (third) bin in Figs. 10 and 11.

The number of differential cross section bins—19—is the number of degrees of freedom in the χ^2 comparisons in Table VII. We see generally good agreement with all three models, but a slight preference for the NuWro prediction that has a lower $\chi^2 = 18.4$ for 19 degrees of freedom. In addition, the χ^2's between the regularized and unregularized cases are seen to be consistent. Hence, we find essentially the same results with and without regularization.

The total cross section integrated over all 19 bins can be determined from the data and compared to NEUT, GENIE, and NuWro predictions. The T2K flux-averaged cross sections, in the kinematic phase space in Table IV, are given in units of 10^{-38} $\frac{\text{cm}^2}{\text{water molecule}}$ as

$$\begin{aligned}
\sigma_{\text{DATA}}^{\text{regularized}} &= 1.11 \pm 0.18, \\
\sigma_{\text{DATA}}^{\text{unregularized}} &= 1.17 \pm 0.22, \\
\sigma_{\text{NEUT}} &= 1.05, \\
\sigma_{\text{GENIE}} &= .954, \\
\sigma_{\text{NuWro}} &= .911.
\end{aligned} \tag{14}$$

A data release has been provided [53] that contains the double-differential cross section central values and associated relative covariance matrix for both the regularized and unregularized fits.

VII. DISCUSSION AND SUMMARY

We have performed a measurement of the $\bar{\nu}_\mu$ CC double-differential cross section on water without pions in the final state averaged over the T2K antineutrino beam flux. The measurement method in momentum-$\cos\theta$ bins included a likelihood fit with unfolding to correct for bin-to-bin smearing. The data was fit without regularization and with regularization to reduce bin-to-bin fluctuations that are possible when using unfolding methods. The regularized and unregularized results were nearly identical. The comparisons with the NEUT, GENIE, and NuWro models found a lowest χ^2 for NuWro where nearly all of the 19 measured data bins agreed within 1 standard deviation of the NuWro predictions.

In summary, the first measurements of antineutrino cross sections on water were presented and found to be in agreement with several MC model predictions including NEUT, which is extensively used in the T2K measurements of antineutrino interactions at the SuperK far detector. These antineutrino measurements and comparisons to Monte Carlo predictions are extremely important for the measurements of the antineutrino oscillation rates and the search for *CP* violation by T2K and for the development of future long-baseline neutrino experiments.

The data related to the results presented in this paper can be found in Ref. [53].

ACKNOWLEDGMENTS

We thank the J-PARC staff for superb accelerator performance. We thank the CERN NA61/SHINE Collaboration for providing valuable particle production data. We acknowledge the support of MEXT, Japan; NSERC (Grant No. SAPPJ-2014-00031), the NRC and CFI, Canada; the CEA and CNRS/IN2P3, France; the DFG, Germany; the INFN, Italy; the National Science Centre and Ministry of Science and Higher Education, Poland; the RSF (Grant No. 19-12-00325) and the Ministry of Science and Higher Education, Russia; MINECO and ERDF funds, Spain; the SNSF and SERI, Switzerland; the STFC, UK; and the DOE, USA. We also thank CERN for the UA1/NOMAD magnet, DESY for the HERA-B magnet mover system, NII for SINET4, the WestGrid and SciNet consortia in Compute Canada, and GridPP in the United Kingdom. In addition, participation of individual researchers and institutions has been further supported by funds from the ERC (FP7), "la Caixa" Foundation (ID 100010434, fellowship code LCF/BQ/IN17/11620050), the European Union's Horizon 2020 Research and Innovation Programme under the Marie Sklodowska-Curie Grants Agreement No. 713673 and No. 754496, and H2020 Grant No. RISE-GA822070-JENNIFER2 2020 and No. RISE-GA872549-SK2HK; the JSPS, Japan; the Royal Society, UK; French ANR Grant No. ANR-19-CE31-0001; and the DOE Early Career programme, USA.

[1] K. Abe *et al.* (T2K Collaboration), Phys. Rev. Lett. **121**, 171802 (2018).
[2] P. Adamson *et al.* (NOvA Collaboration), Phys. Rev. Lett. **118**, 151802 (2017).
[3] K. Abe *et al.* (T2K Collaboration), Nucl. Instrum. Methods Phys. Res., Sect. A **659**, 106 (2011).
[4] P. Adamson *et al.* (NOvA Collaboration), Phys. Rev. Lett. **116**, 151806 (2016).
[5] R. Acciarri *et al.* (DUNE Collaboration), arXiv:1512.06148.
[6] K. Abe *et al.* (Hyper-Kamiokande Working Group), arXiv:1412.4673.
[7] R. A. Smith and E. J. Moniz, Nucl. Phys. **B43**, 605 (1972); **B101**, 547(E) (1975).
[8] O. Benhar, A. Fabrocini, S. Fantoni, and I. Sick, Nucl. Phys. **A579**, 493 (1994).
[9] A. M. Ankowski, O. Benhar, and N. Farina, Phys. Rev. D **82**, 013002 (2010).
[10] S. K. Singh and E. Oset, Nucl. Phys. **A542**, 587 (1992).
[11] A. Gil, J. Nieves, and E. Oset, Nucl. Phys. **A627**, 543 (1997).
[12] J. Nieves, J. E. Amaro, and M. Valverde, Phys. Rev. C **70**, 055503 (2004); **72**, 019902 (2005).
[13] J. Nieves, M. Valverde, and M. J. Vicente Vacas, Phys. Rev. C **73**, 025504 (2006).
[14] R. Gran, J. Nieves, F. Sanchez, and M. V. Vacas, Phys. Rev. D **88**, 113007 (2013).
[15] M. Martini, M. Ericson, G. Chanfray, and J. Marteau, Phys. Rev. C **80**, 065501 (2009).
[16] J. Delorme and M. Ericson, Phys. Lett. **156B**, 263 (1985).
[17] J. Marteau, J. Delorme, and M. Ericson, Nucl. Instrum. Methods Phys. Res., Sect. A **451**, 76 (2000).
[18] M. Martini, M. Ericson, G. Chanfray, and J. Marteau, Phys. Rev. C **81**, 045502 (2010).
[19] J. Nieves, I. Ruiz Simo, and M. J. Vicente Vacas, Phys. Lett. B **707**, 72 (2012).
[20] M. Martini, M. Ericson, and G. Chanfray, Phys. Rev. C **84**, 055502 (2011).
[21] J. Nieves, I. R. Simo, and M. V. Vacas, Phys. Lett. B **707**, 72 (2012).
[22] O. Buss, T. Gaitanos, K. Gallmeister, H. van Hees, M. Kaskulov, O. Lalakulich, A. B. Larionov, T. Leitner, J. Weil, and U. Mosel, Phys. Rep. **512**, 1 (2012).
[23] K. Gallmeister, U. Mosel, and J. Weil, Phys. Rev. C **94**, 035502 (2016).
[24] G. D. Megias, J. E. Amaro, M. B. Barbaro, J. A. Caballero, and T. W. Donnelly, Phys. Rev. D **94**, 013012 (2016).
[25] K. Abe *et al.* (Hyper-Kamiokande Proto-Collaboration), Prog. Theor. Exp. Phys. **2015**, 53C02 (2015).
[26] K. Abe *et al.* (T2K Collaboration), Phys. Rev. D **96**, 052001 (2017).
[27] K. Abe *et al.* (T2K Collaboration), Phys. Rev. D **93**, 112012 (2016).
[28] K. Abe *et al.* (T2K Collaboration), Phys. Rev. D **97**, 012001 (2018).
[29] K. Abe *et al.* (T2K Collaboration), Phys. Rev. D **90**, 052010 (2014).
[30] K. Abe *et al.* (T2K Collaboration), Phys. Rev. D **93**, 072002 (2016).
[31] K. Abe *et al.* (T2K Collaboration), Prog. Theor. Exp. Phys. **2019**, 093C02 (2019).
[32] K. Abe *et al.* (T2K Collaboration), Phys. Rev. D **98**, 032003 (2018).
[33] K. Abe *et al.* (T2K Collaboration), Phys. Rev. D **87**, 012001 (2013).
[34] T. Bohlen, F. Cerutti, M. Chin, A. Fasso, A. Ferrari, P. Ortega, A. Mairani, P. Sala, G. Smirnov, and V. Vlachoudis, Nucl. Data Sheets **120**, 211 (2014).
[35] A. Ferrari, P. R. Sala, A. Fasso, and J. Ranft, Report No. CERN-2005-010, SLAC-R-773, INFN-TC-05-11 FLUKA transport code.
[36] R. Brun, F. Carminati, and S. Giani, Report No. CERN-W5013 (1994).
[37] C. Zeitnitz and T. A. Gabriel, Nucl. Instrum. Methods Phys. Res., Sect. A **349**, 106 (1994).
[38] N. Abgrall *et al.* (NA61/SHINE Collaborations), Phys. Rev. C **84**, 034604 (2011).
[39] N. Abgrall *et al.* (NA61/SHINE Collaborations), Phys. Rev. C **85**, 035210 (2012).
[40] N. Abgrall *et al.* (NA61/SHINE Collaborations), Eur. Phys. J. C **76**, 84 (2016).
[41] K. Abe *et al.* (T2K Collaboration), Phys. Rev. D **96**, 092006 (2017).
[42] S. Assylbekov *et al.* (T2K ND280 P0D Collaboration), Nucl. Instrum. Methods Phys. Res., Sect. A **686**, 48 (2012).
[43] N. Abgrall *et al.* (T2K ND280 TPC Collaboration), Nucl. Instrum. Methods Phys. Res., Sect. A **637**, 25 (2011).
[44] Y. Hayato, Acta Phys. Pol. B **40**, 2477 (2009). https://www.actaphys.uj.edu.pl/fulltext?series=Reg&vol=40&page=2477
[45] S. Agostinelli *et al.* (GEANT4 Collaboration), Nucl. Instrum. Methods Phys. Res., Sect. A **506**, 250 (2003).
[46] G. Folger, http://geant4-userdoc.web.cern.ch/geant4-userdoc/UsersGuides/PhysicsListGuide/html/index.html.
[47] S. Baker and R. D. Cousins, Nucl. Instrum. Methods Phys. Res., Sect. A **221**, 437 (1984).
[48] K. Abe *et al.* (T2K Collaboration), Phys. Rev. D **96**, 011102 (2017).
[49] K. Abe *et al.* (T2K Collaboration), Phys. Rev. D **91**, 112002 (2015).
[50] D. Calvetti, S. Morigi, L. Reichel, and F. Sgallari, J. Comput. Appl. Math. **123**, 423 (2000).
[51] P. C. Hansen, SIAM Rev. **34**, 561 (1992).
[52] P. Stowell *et al.*, J. Instrum. **12**, P01016 (2017).
[53] http://t2k-experiment.org/results/data-release-for-the-measurement-of-the-charged-current-electron-anti-neutrino-inclusive-cross-sections-at-the-t2k-off-axis-near-detector-nd280.